Citation (APA)
Al-Mashharawi, S. K., Steele-Dunne, S. C., El Hajj, M. M., Valencia, O. M. L., Camargo, O. A. L., Pouget, G., Doussan, C., Courault, D., & McCabe, M. F. (2026). Exploring the use of thermal neutron counts to track orchard phenological development. *Frontiers in Water*, *8*, Article 1749654. https://doi.org/10.3389/frwa.2026.1749654

frontiers in Water

TYPE Original Research
PUBLISHED 26 February 2026
DOI 10.3389/frwa.2026.1749654

Exploring the use of thermal neutron counts to track orchard phenological development

Samer K. Al-Mashharawi[1,2]*, Susan C. Steele-Dunne[2], Marcel M. El Hajj[1], Oliver M. López Valencia[1], Omar A. López Camargo[1], Guillaume Pouget[3], Claude Doussan[3], Dominique Courault[3] and Matthew F. McCabe[1]

[1]Hydrology, Agriculture and Land Observation (HALO) Laboratory, Division of Biological and Environmental Sciences and Engineering, King Abdullah University of Science and Technology (KAUST), Thuwal, Saudi Arabia, [2]Department of Geoscience and Remote Sensing, Delft University of Technology, Delft, Netherlands, [3]INRAE, Avignon University, UMR EMMAH, Avignon, France

EDITED BY
Kristian Förster,
Weihenstephan-Triesdorf University of Applied Sciences, Germany

REVIEWED BY
Heye Reemt Bogena,
Helmholtz Association of German Research Centres (HZ), Germany
Markus Köhli,
Heidelberg University, Germany

*CORRESPONDENCE
Samer K. Al-Mashharawi
✉ samir.mashharawi@kaust.edu.sa

RECEIVED 19 November 2025
REVISED 02 February 2026
ACCEPTED 03 February 2026
PUBLISHED 26 February 2026

CITATION
Al-Mashharawi SK, Steele-Dunne SC, El Hajj MM, Valencia OML, Camargo OAL, Pouget G, Doussan C, Courault D and McCabe MF (2026) Exploring the use of thermal neutron counts to track orchard phenological development.
Front. Water 8:1749654.
doi: 10.3389/frwa.2026.1749654

Regular monitoring of plant development and soil moisture variations is essential for managing orchard systems and optimizing irrigation. Cosmic Ray Neutron Sensors (CRNS) are increasingly used for reliable, non-invasive soil moisture estimation. However, the potential of CRNS for monitoring plant development remains largely uninvestigated. The objective of this study is to assess the response of thermal (N_{th}) and epithermal (N_{epi}) neutron intensities to the seasonal changes in tree structure and water content. In particular, we aim to investigate whether the observed neutron responses can be used as an indicator of plant development in commercial orchard settings. A CRNS was installed at a cherry orchard site in southeastern France and operated continuously for 10 months in 2022. Observations were compared to several proxies for tree canopy characteristics. First, neutron intensity values were compared with monthly plant area index (PAI) estimates derived from images collected with a light detection and ranging (LiDAR) sensor mounted on an unmanned aerial vehicle (UAV). PAI in (m^2 m^{-2}) is defined as the total surface area of all above-ground canopy components, including leaves, stems, and branches per unit horizontal ground surface area. Second, N_{th} was compared with commonly used vegetation indices derived from multispectral satellite images acquired by PlanetScope and Sentinel-2. The results show a strong correlation between N_{th} and UAV-derived PAI with $R^2 = 0.86$. N_{th} increased linearly by approximately 4.5% per 1 m^2 m^{-2} increase in PAI. Of the vegetation indices, the Normalized Difference Red Edge (NDRE) index derived from PlanetScope images showed the highest correlation ($R^2 = 0.69$) with N_{th}. The corresponding R^2 with NDRE from coarser-resolution Sentinel-2 data was lower ($R^2 = 0.51$). The correlation between N_{th} and PAI was higher than that between N_{th} and SM ($R^2 = 0.61$). Results suggest that variations in N_{th} are potentially valuable for vegetation monitoring, provided the confounding effect of soil moisture can be taken into account.

KEYWORDS
cosmic ray neutron sensor (CRNS), orchard phenology monitoring, PlanetScope, plant area index, Sentinel-2, thermal neutron counts, UAV-LiDAR, vegetation indices

1 Introduction

Cosmic-Ray Neutron Sensors (CRNS) are becoming increasingly common for soil moisture estimation due to their ability to provide non-invasive measurements at the hectare scale (Zreda et al., 2012). CRNS networks have been established worldwide including COSMOS network in the US (Zreda et al., 2012), COSMOS-Australia (CSIRO, 2010), COSMOS-UK (Cooper et al., 2021), COSMOS-India (Upadhyaya et al., 2021), and several sub-networks and individual sensors across Europe (Bogena et al., 2022). Data from many of these networks are accessible through the International Soil Moisture Network (2025) (Dorigo et al., 2021). CRNS networks are primarily used for soil moisture monitoring across a wide range of environments, from bare soil and croplands to vegetated and forested ecosystems. However, the presence of vegetation affects CRNS measurements due to the water present in the leaves, fruits, and stems, with the effect depending on vegetation type and structure (Andreasen et al., 2017). For some CRNS installations, soil moisture retrievals have been improved by accounting for the impact of vegetation on epithermal neutron counts using *in situ* measurements of biomass water equivalent (BWE) (Baatz et al., 2015; Franz et al., 2018). Hydrogen in vegetation interacts with neutrons and reduces their energy levels and intensities. This can contribute to an over- or underestimation of soil moisture estimates if not properly accounted for (Andreasen et al., 2016; Baroni and Oswald, 2015; Jakobi et al., 2022). However, due to the complexity of biomass corrections and the need for additional vegetation information, their implementation is limited. As a result, vegetation artifacts sometimes remain in CRNS soil moisture estimates, despite the availability of correction methods (Baroni and Oswald, 2015; Jakobi et al., 2018; Morris et al., 2024; Baatz et al., 2015). While the sensitivity of neutron counts to water in vegetation is a challenge for soil moisture estimation, it provides an opportunity for vegetation monitoring.

To date, vegetation effects on CRNS signals have primarily been studied in the context of accounting for their impact in soil moisture estimation. Most studies determine BWE through multiple destructive sampling and then relate these variations to CRNS measurements (Franz et al., 2018; Jakobi et al., 2022; Morris et al., 2024; Vather et al., 2020). Baatz et al. (2015) found a 0.9% reduction in epithermal neutron counts for every 1 kg/m^2 of BWE, and based on that, developed a vegetation correction by optimizing the site-specific calibration parameter N_0 (the reference neutron count rate under dry soil conditions). An alternative approach used the neutron ratio (Nr) i.e., $\frac{N_{\text{thermal}}}{N_{\text{epithermal}}}$, to account for vegetation effects on epithermal intensity and improve soil moisture estimates (Tian et al., 2016; Jakobi et al., 2018). The neutron ratio was used because it shows a linear relationship with BWE throughout the growing season (Tian et al., 2016; Jakobi et al., 2018). However, Jakobi et al. (2022) found that the neutron ratio-to-biomass relation is sensitive to other hydrogen pools, is vegetation-specific and may not be transferable to other vegetation types without adjustments. Despite several studies quantifying vegetation effects on neutron fluxes, their direct use for vegetation monitoring remains relatively unexplored, particularly in orchard settings.

In this study, we build on recent findings that have explored the potential of N_{th} to estimate biomass effects on CRNS signals. Jakobi et al. (2022) demonstrated that thermal neutron intensity can be used to correct for biomass effects in soil moisture measurements. More recently, Brogi et al. (2025) showed that time series of thermal neutron counts can be used to estimate several vegetation properties, such as plant height, leaf area index and dry above-ground biomass, for various crop types. They also compared N_{th} derived vegetation properties with those derived from LiDAR and multispectral drone data. Although both thermal and epithermal neutrons are influenced by hydrogen, thermal neutrons are potentially more sensitive to biomass (e.g., plant carbohydrates and structural material) (Jakobi et al., 2022). Therefore, in deciduous systems such as cherry orchards, the impact of seasonal leaf development and senescence can be greater on thermal neutron intensity than on epithermal neutrons, although soil moisture remains the main driver of both signals. N_{th}, with energies typically below $\approx$0.5 eV, are more sensitive to crop biomass than soil water content and interact with vegetation in a way that results in an increase in its counts in areas with denser vegetation cover (Jakobi et al., 2022). When epithermal neutrons (with energies ranging from $\approx$0.5 eV to 100 keV) pass through vegetation, they lose energy through interactions with hydrogen atoms in leaves and stems (Andreasen et al., 2020; Bogena et al., 2013), this interaction results in reduced epithermal neutron intensity and increased thermal neutron counts in regions with denser vegetation (Vather et al., 2020). For instance, Vather et al. (2020) found that following clear-felling of an Acacia forest (tree heights 15–21 m), epithermal neutron intensity increased while thermal neutron intensity decreased. The hydrogen in above-ground biomass is highly effective at moderating epithermal neutrons, which in turn leads to increased production of thermal neutrons compared to bare soil conditions, where neutrons moderation is primarily controlled by soil moisture alone (Brogi et al., 2025). On the other hand, epithermal neutrons are more sensitive to soil moisture and other hydrogen sources, such as atmospheric humidity.

Existing biomass correction methods have been developed primarily for annual crops (Morris et al., 2024; Franz et al., 2018; Baroni and Oswald, 2015) or heterogeneous forests (Wang et al., 2023; Bogena et al., 2013; Baatz et al., 2015), with few applications in orchard settings (Brogi et al., 2023; Li et al., 2019). In these few orchard-related studies, the empirical correction factors relied on destructive biomass samples. Perennial orchard systems have distinct characteristics that necessitate a dedicated approach to account for biomass changes. For instance, while annual crops such as maize and soybeans experience rapid and relatively uniform biomass changes over short growing seasons, commercial orchards undergo slower and more gradual biomass development because of their perennial nature. At harvest, annual crops are usually completely removed, whereas in orchards, only the fruit is harvested while the majority of the tree, its woody biomass, remains to store water and support the structure. Compared to commercial orchards, dense forests have taller trees, a mix of different vegetation types, and dense canopy structures, while commercial orchards consist of widely spaced trees with semi-uniform canopy structures. Our recent study showed that the annual phenological dynamics in orchards can influence CRNS signals and compromise the accuracy of soil moisture estimation (Al-Mashharawi et al., 2025).

The motivation for this study is to exploit the observed sensitivity of CRNS signals, specifically N_{th}, to monitor plant development in commercial perennial orchards. This study examines how N_{th} varies in response to biomass changes during a growing season in a commercial perennial orchard. Time series of N_{th} measurements were compared with temporally sparse but high-precision UAV-LiDAR-derived plant area index (PAI). Additionally, satellite-derived vegetation indices and estimated leaf area index (LAI) were analyzed from PlanetScope and Sentinel-2, which provide more frequent observations but with coarser spatial resolution.

2 Materials and methods

2.1 Research site

The study was carried out on a 4.8-hectare cherry orchard located in the Provence-Alpes-Côte d'Azur region of southeastern France, centered at (44°11′34.8″N, 5°09′24.4″E), see Figure 1. The area has a Mediterranean climate, characterized by hot and dry summers with average daily temperatures around 30 °C, and cold winters with an average daily temperature below 10 °C. Annual precipitation ranges from 650 to 900 mm, with heavy rains usually occurring in September and October (Rouault et al., 2024). The orchard is organized into rows with a 7 m spacing and 5.5 m between trees, with wild grass covering the inter-row spaces. In 2022, the grass was mowed twice, late April and late May, and then left to dry out. Re-greening of the inter-row grass was observed starting in early September, followed by slow subsequent growth. The orchard contains five varieties of cherry: Prime-Giant, Belge, Belise, Folfer, and Summit, planted to provide early, mid, and late season yields to ensure a prolonged harvest period of approximately 40 days. The trees are planted at a density of 240 trees per hectare, with an average canopy dimension of 5.9 m (length) × 5.3 m (width) × 3.5 m (height). This corresponds to a tree density of 0.024 trees per square meter. The orchard is equipped with a drip irrigation system with a designed flow rate of 31.4 L per hour per tree. The irrigation system operated for 6 h per week in April, increased to between 1 and 3 h per day during May, June, July, and mid-August, and then was reduced to between 3 and 10 h per week, based on weather conditions and local authority regulations. A data logger was installed near the center of the orchard to collect *in situ* soil moisture data. Cherry trees were pruned and thinned in mid-November, and all work was completed by the end of November.

2.2 Cosmic ray neutron sensor (CRNS)

The CRNS used in this research is the CRS2000B from Hydroinnova LLC (2024). The system consists of two detector tubes, each approximately 1.5 m tall and filled with boron trifluoride gas for high neutron absorption. One detector is moderated by a 2.5 cm thick polyethylene layer (moderated detector), while the other remains unmoderated (bare detector). When neutrons enter the tubes, some are absorbed by the gas and generate electrical signals that are recorded. The bare detector measures low energy (thermal neutrons), while the moderated detector measures higher energy (epithermal neutrons). In February 2022, the CRNS was installed in the middle of the cherry orchard, mounted on a stand at 50 cm height. The bottoms of the detectors align with the bottom of the canopy, and the tops of the detectors are still below the average canopy height (around 3.5 m). A data logger records the total neutron count as well as with the average temperature, relative humidity, barometric pressure, and total rain data.

The raw neutron (N_{raw}) data are collected in hourly intervals and reported in units of counts per hour (cph). Before analysis, the raw data undergo a series of filtering and correction steps to remove invalid measurements and account for the influence of environmental variables. Outliers in N_{raw} data were removed following established CRNS data pre-processing protocols. Specifically, outliers (i.e., $N_{\mathrm{raw}} < 50$ cph or $N_{\mathrm{raw}} >$ 10,000 cph) and values exceeding the 24-h rolling mean by more than twice the standard deviation were excluded (Bogena et al., 2022). After outlier removal, correction factors were applied following (Zreda et al., 2012):

$$N = N_{\mathrm{raw}} \cdot f_p \cdot f_i \cdot f_h \tag{1}$$

where f_{p}, f_{i}, and f_{h} are the correction parameters for atmospheric pressure variations, incoming cosmic-ray neutron intensity variation (Zreda et al., 2012) and atmospheric water vapor (Rosolem et al., 2013), respectively. The correction applied for incoming cosmic-ray neutron intensity accounts for elevation and geomagnetic latitude using the scaling approach of McJannet and Desilets (2023).

Some studies suggest correcting thermal neutron counts only for atmospheric pressure and absolute humidity (Jakobi et al., 2018). Sensitivity analyses without the incoming neutron correction showed no major impact on the relationship between thermal neutron counts and vegetation metrics. These results are presented in the Supplementary Figures S8, S9. In addition, recent studies by Schrön et al. (2024) and Rasche et al. (2023) proposed that the water vapor correction factor for thermal neutrons is approximately 40% of the value used for epithermal neutrons. Therefore, following Schrön et al. (2024), the water vapor correction factor was adjusted from the standard correction factor (0.0054 $\mathrm{m}^3\,\mathrm{g}^{-1}$) to the reduced factor (0.0021 $\mathrm{m}^3\,\mathrm{g}^{-1}$) for thermal neutrons. The factors are calculated using the following equations:

$$f_i = \frac{I_{\mathrm{ref}}}{I} \tag{2}$$

$$f_h = 1 + \alpha\,(h - h_0) \tag{3}$$

where the coefficient α is:

$$\alpha = \begin{cases} 0.0021 & \text{for thermal neutrons,} \\ 0.0054 & \text{for epithermal neutrons,} \end{cases}$$

$$f_p = \exp\left(\beta(P - P_0)\right) \tag{4}$$

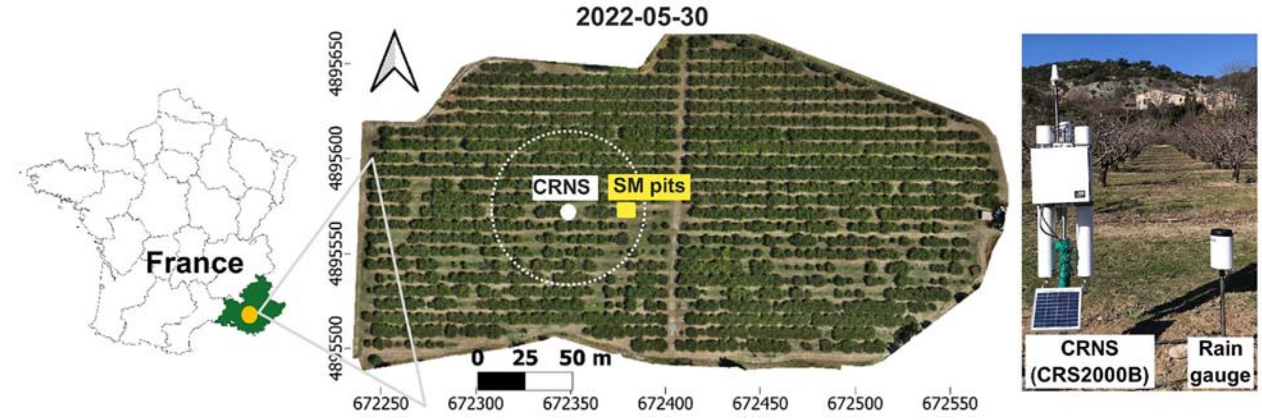

FIGURE 1
Location of the cherry orchard site in southeastern France, showing the CRS2000B Cosmic Ray Neutron Sensor and the locations of the *in situ* soil moisture pits. The right image shows a rain gauge beside the CRNS, which consists of bare and moderated detectors, a data logger and integrated temperature, humidity and pressure sensors. The aerial orthomosaic image (center) was captured using a 20-MP camera on a Matrice-300 UAV system and reconstructed using Agisoft Metashape software. France map (left) derived from Natural Earth (version 5.1.1, public domain, naturalearthdata.com).

where I ($\mathrm{cts\,s^{-1}}$) is the neutron intensity measured by the Jungfraujoch (JUNG) monitoring station in Switzerland (available at www.nmdb.eu) at a given time, and I_{ref} ($\mathrm{cts\,s^{-1}}$) is an arbitrary reference value used for normalizing cosmic-ray intensity data. In this study, I_{ref} was set to 159.4 ($\mathrm{cts\,s^{-1}}$), the daily average measured at Jungfraujoch on 2011-05-01. h is the absolute air humidity ($\mathrm{g\,cm^{-3}}$) and h_0 ($\mathrm{g\,cm^{-3}}$) is the average air humidity over the study period. P is the measured air pressure (mbar) and P_0 is the average pressure over the study period. The neutron barometric coefficient, β, was estimated using a tool developed by CRNSLAB using the calculation described in McJannet and Desilets (2023) (available at crnslab.org/util/intensity.php) and has a value of 136 $\mathrm{mbar^{-1}}$ at the study site. Lastly, daily mean N_{epi} and N_{th} values were calculated to compare to the UAV-LiDAR-derived PAI and satellite-derived vegetation indices. The daily means were computed from the hourly CRNS data, and the daily standard deviation is considered an indication of uncertainty.

2.3 *In situ* soil moisture data

Six HydraProbe-II sensors (Stevens Water Monitoring Systems Inc., Portland, Oregon, USA) were installed approximately 40 m from the CRNS and collected soil moisture data every 30 min. Their location is indicated by the orange rectangle in Figure 1. The sensors were divided into two sets, each consisting of three sensors installed at 5, 15, and 30 cm depths. One set was installed within the tree rows, to represent the irrigated portion of the field which accounts for 17% of the field area. The other set was installed in the inter-row spaces, which represents the remaining 83% (non-irrigated) field area.

The mean soil moisture value at each depth was calculated using area-based weights of 17 and 83% before calculating a daily mean. To account for depth-related contributions to the cosmic-ray neutron signal, the weighting approach proposed by Schrön et al. (2017) was applied using weights of 0.7, 0.25, and 0.05 for the 5, 15, and 30 cm layers, respectively.

2.4 Plant area index (PAI) estimation using UAV LiDAR data

Plant development in this study was primarily quantified using the plant area index (PAI), derived from UAV (Unmanned Aerial Vehicle)-based LiDAR (light detection and ranging) data. UAV-based LiDAR provides unique three dimensional canopy structure information that can be used to calculate PAI. PAI ($\mathrm{m^2\ m^{-2}}$) is defined as the surface area of all above-ground plant components per unit of ground area. It includes both green and non-green leaves as well as woody parts of the plant, such as stems and branches (Jonckheere et al., 2004). PAI is widely used for vegetation monitoring and modeling purposes (Grau et al., 2017). UAV-LiDAR data are suitable for estimating tree structural properties such as height, and canopy volume and density (Farhan et al., 2024). However, data collection is labor-intensive and time-consuming. Although it does not provide a direct estimate of vegetation water content, variations in height, canopy volume and leaf density provide a measure of changes in above ground biomass and hence water content, which influences hydrogen and neutron counts. PAI is therefore used to characterize canopy development throughout the phenological cycle of the orchard.

UAV-based LiDAR data were acquired in 2022 with at least one acquisition per month. The UAV-LiDAR system used was a DJI Matrice 300 RTK quadcopter (DJI Technology Co., Ltd., 2020) equipped with a DJI L1 LiDAR sensor (DJI Technology Co., Ltd., 2021). The flights were carried out at an altitude of 50 m, with a velocity of 2.5 m $\mathrm{s^{-1}}$ and a 50% side overlap to ensure complete coverage of the orchard and providing a point density of roughly 3,300 points $\mathrm{m^{-2}}$. Each laser pulse emitted by the LiDAR sensor can generate up to three returns, reflecting from different layers of the canopy such as leaves, branches, or the ground. This multi-return capability helps to capture the vertical structure of the trees. Additionally, a real-time kinematic (RTK) system was utilized for georeferencing, supplemented with nine Ground Control Points (GCPs) to enhance positional accuracy. The UAV was also equipped with a DJI Zenmuse P1 RGB camera (DJI Technology Co., Ltd.,

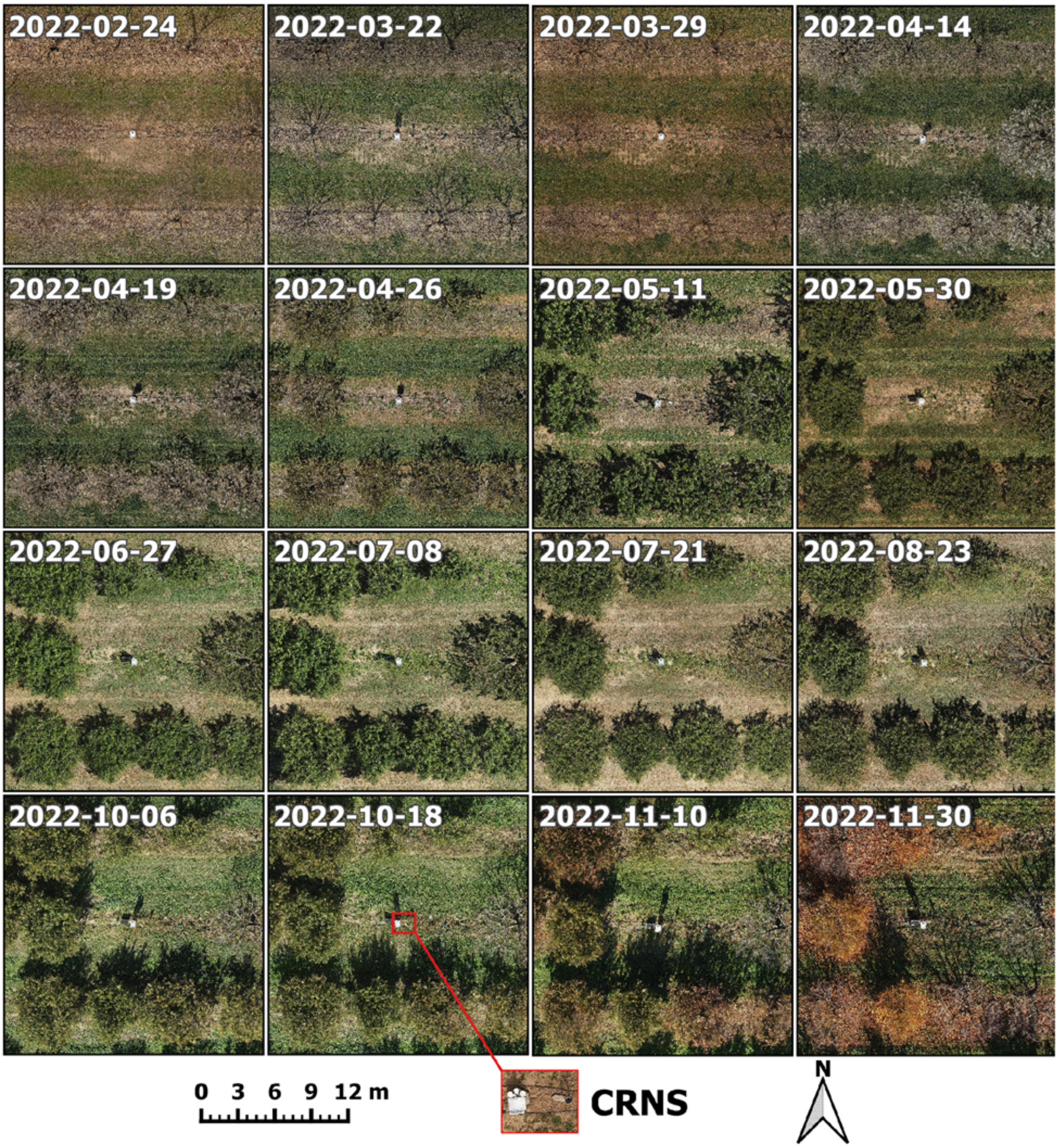

FIGURE 2
Phenological changes of the cherry orchard from February to December 2022. Images were captured by the 20-MP camera integrated with the UAV-mounted LiDAR system. The CRNS is positioned near the center of each image.

2019). The photos were processed with Agisoft Metashape software (Agisoft, 2024) for geometric rectification and photogrammetry, resulting in detailed orthomosaics of the orchard. The RGB images collected during the campaign capture the progression of tree phenological stages throughout the year, from leafless to full canopy development and back to leafless (see Figure 2). Figure 2 highlights the main transitions in canopy phenology, including dormancy (February–March), flowering (April), fruit growth (May–June), fruit ripening and harvest (July–August), and leaf senescence (October–December).

A voxel-based method was used to estimate PAI from the UAV-LiDAR data. The point cloud was processed using the open-source `leafR` package (version 0.3.5), which was developed to map canopy metrics, including PAI and height using a voxel-based approach (Almeida et al., 2021). The point cloud was represented in a grid of 3-dimentional cubes (voxels), and PAI was estimated for each voxel. PAI was estimated using an application of the Beer–Lambert law to relate canopy density to the attenuation of radiation through vegetation. For the discrete-return LiDAR data, cumulative PAI at a given canopy depth was derived by approximating light attenuation as the ratio of LiDAR pulses entering and exiting successive canopy layers (i.e., voxels), following Bouvier et al. (2015). To compute PAI in each voxel, the acquired point cloud data were structured into a 3D voxel grid (70 cm × 70 cm × 30 cm) using the x, y, z coordinates of each LiDAR return. The voxel size of 70 cm × 70 cm was chosen to maximize the number of LiDAR points used for PAI estimation given the average canopy dimension of approximately 5.3 m × 6 m. Then, for each column of voxels, the number of points within each voxel (from voxel 1 to voxel n) was calculated. PAI was estimated for each voxel (voxel i) as the ratio of the cumulative number of points from the top voxel down to voxel i (voxels 1 to i) to the cumulative number of points from voxel i + 1 to the bottom voxel (voxels i + 1 to n). The PAI for each column was then calculated as the sum of the individual voxel-based PAI values in that column. The outcome was a PAI map for the entire plot with a horizontal resolution of 70 cm × 70 cm. Previous studies have shown that 86% of the measured thermal neutrons were thermalized within a radial distance of 43–48 m from the CRNS (Jakobi et al., 2021). Therefore, voxel-based PAI values within a 45 m radius of the CRNS were averaged for comparison with thermal neutron counts.

2.5 PlanetScope and Sentinel-2 satellites data

Multispectral satellite data are also employed to provide additional insights into the orchard phenology and development. While satellite indices primarily capture signals from the top canopy surface, their broad spatial coverage and frequent revisit times make them highly suitable for vegetation monitoring. Satellite remote sensing data are widely used to derive vegetation indices such as normalized difference vegetation index (NDVI), normalized difference water index (NDWI), and normalized difference red edge (NDRE), which can be used to assess canopy condition and estimate biomass. The leaf area index (LAI), which is the ratio of the green leaf area to the ground area (in $m^2\ m^{-2}$), can be estimated from these indices.

A total of 164 cloud-free PlanetScope SuperDove surface reflectance images were collected during the UAV survey period between February 15 and December 1, 2022. These images were downloaded from the Planet Explorer platform (Planet Labs Inc., 2023) and clipped to a radius of 45 m around the CRNS to match the average footprint of the N_{th} detector (Jakobi et al., 2021, 2022). For days with multiple image acquisitions, the images were averaged, resulting in 98 images being retained for analysis. The data include eight spectral bands (i.e., red edge, red, green, green I, yellow, blue, coastal blue, and near-infrared) with a spatial resolution of 3 m.

In addition, the images were harmonized with Sentinel-2 using the "harmonize" imagery option available in Planet Explorer to ensure the spectral consistency of the vegetation indices (Kington and Collison, 2022; Houborg and McCabe, 2018). This approach corrects for the difference in surface reflectance between PlanetScope and Sentinel-2 common bands (Green, Red, Red Edge, and Near-Infrared), due to differences in sensor wavelength characteristics as provided in Table 1 (Baldin and Casella, 2024; Houborg and McCabe, 2016) .

TABLE 1 Comparison of PlanetScope and Sentinel-2 wavelengths for common bands.

Band	PlanetScope	Sentinel 2
Green	G1 (500–520 nm)	3 (560 nm)
Red	R (665–685 nm)	4 (665 nm)
Red edge	RE (705–725 nm)	5 (704 nm)
Near-infrared (NIR)	NIR (820–860 nm)	8 [835.1 nm (S2A)/833 nm (S2B)]

Surface reflectance Level 2 Sentinel-2 imagery was obtained via the Google Earth Engine, following the correction procedure outlined in (Hagolle et al., 2008). Imagery was obtained from February to December 2022, with a temporal resolution ranging between 3 and 6 days. Due to cloud cover, a total of 76 suitable images were available during the 11-month study period. The resolution of Sentinel-2 images is 10 m for the green, red and NIR images, and 20 m for the red edge band (European Space Agency, 2020).

2.6 Vegetation indices calculation from PlanetScope and Sentinel-2 data

Four key vegetation indices (Normalized Difference Vegetation Index "NDVI," Normalized Difference Red Edge Index "NDRE," Normalized Difference Water Index "NDWI," and Leaf Area Index "LAI") were calculated from both PlanetScope and Sentinel-2 data. These indices (Equations 5–7) are computed using common spectral bands common to both sensors (Near-Infrared, Red, Green, and Red Edge), and are commonly used in vegetation monitoring. The NDVI is widely used to assess vegetation health and is calculated as follows:

$$\mathrm{NDVI} = \frac{\mathrm{NIR} - \mathrm{Red}}{\mathrm{NIR} + \mathrm{Red}}, \tag{5}$$

where NIR is the near-infrared reflectance and Red is the red band reflectance. The NDWI relates to vegetation water content and is calculated as:

$$\mathrm{NDWI} = \frac{\mathrm{NIR} - \mathrm{Green}}{\mathrm{NIR} + \mathrm{Green}}, \tag{6}$$

where Green is green band reflectance. NDWI has been shown to be more sensitive to canopy water content and biomass (Contreras et al., 2025). NDRE is sensitive to chlorophyll content and detects early plant stress before it is visible in NDVI, using a narrower red-edge waveband and calculated as:

$$\mathrm{NDRE} = \frac{\mathrm{NIR} - \mathrm{RedEdge}}{\mathrm{NIR} + \mathrm{RedEdge}}, \tag{7}$$

where RedEdge is red-edge band reflectance. The use of these indices is based on their correlations with field-measured biomass in orchard systems (Panumonwatee et al., 2025).

Leaf Area Index (LAI) provides a measure of canopy density (Tian et al., 2023), and was estimated from Sentinel-2 and PlanetScope images using the neural network-based algorithm of biophysical variables (BVNet) (Weiss et al., 2002). This algorithm uses reflectances from three spectral bands B3 (Green), B4 (Red), and B8 (Near Infrared) and incorporates solar and sensor angles to refine LAI estimations (Courault et al., 2021). The algorithm utilizes a neural network that has been trained on simulated spectral reflectance, using the SAIL radiative transfer model as described in Weiss et al. (2002). Mukhtar et al. (2022) found that the LAI obtained through the BVNet algorithm was capable of tracking the dynamics of leaf development. Based on satisfactory evaluations of BVNet against ground-based measurements performed by Courault et al. (2021), BVNet has been incorporated into the ESA (European Space Agency) S2 toolbox (Abubakar et al., 2023).

2.7 Thermal neutron counts and vegetation indices

Thermal neutron counts were correlated with each of the satellite data-based vegetation indices and the LiDAR-based PAI, and the goodness of fit was evaluated using the determination coefficient (R^2). As demonstrated by Jakobi et al. (2021), approximately 45% of thermal neutrons originate from within a 5 m radius of the detector, with 86% of cumulative contributions coming from a radial footprint of about 45 m. Supplementary Figures S1–S4 show results obtained assuming smaller plot radii around the CRNS (10 and 25 m), and show that the correlation increases as the footprint is increased to this value. Therefore, results in the following section are based on a radial footprint of 45 m.

3 Results and discussion

3.1 Spatial patterns of PAI from UAV LiDAR across the orchard

Representative maps of UAV LiDAR-derived PAI are shown in Figure 3 at both individual tree (panel i) and footprint scales (panel ii) to highlight the spatial variability in PAI across different times of the year. The images in Figure 3i visualizes the three-dimensional LiDAR point clouds for an individual tree at three key phenological stages. The X and Y-axes represent relative horizontal coordinates in meters, used to illustrate the spatial extent and dimensions of the tree rather than absolute geographic position. The Z-axis represents canopy height in meters. On 2022-03-29 (dormancy), the tree consists of a sparse structure with minimal foliage. By 2022-05-30 (ripening period), the canopy has developed into a dense structure with nearly maximum leaf coverage. On 2022-12-01 (post-senescence), the tree returns to a bare structure with only woody elements. PAI maps at the CRNS footprint scale are shown in Figure 3ii with X and Y-axes representing the relative coordinates in meters (X = east-west, Y = north-south), with the CRNS located at the center. On 2022-05-30 (Figure 3ii-a) when leaves are fully developed and fruit is approximately halfway through ripening, PAI values are high across the orchard. Individual trees are discernible, with peak values up to 5.8 $m^2\ m^{-2}$ near the canopy center and decreasing PAI with distance from the trunk due to the decrease in branch density. In contrast, on 2022-12-01 (Figure 3ii-b) PAI is uniformly low $<$0.7 $m^2\ m^{-2}$ after senescence and pruning. At this stage, the PAI captures the woody structural elements of the trees. In both maps, the white areas indicate zones of “no data" where the PAI of the canopy is zero due to gaps in the canopy cover. In these zones, the short inter-row vegetation (grass) is located entirely within the bottom voxel making it impossible to obtain a reliable estimate of PAI.

3.2 Neutron response to vegetation and soil moisture variations

Figure 4 shows the *in-situ* rainfall and soil moisture, observed PAI and neutron counts during the study period. Soil moisture (Figure 4a) exhibits some seasonal variation, with values around 0.30 $m^3\ m^{-3}$ during the winter and spring months (January–April), followed by a gradual decline to approximately 0.10–0.15 $m^3\ m^{-3}$ during the summer period. Several rainfall events occurred throughout the year (indicated by gray bars). The larger rainfall events produce soil moisture drydowns in April, July, and September. Vegetation growth stage is indicated in Figure 4a. The PAI in the 45 m CRNS footprint is lowest during dormancy (0.5 $m^2\ m^{-2}$) and increases from early spring (March) to reach its peak during early summer (end of June) (2.8 $m^2\ m^{-2}$) when the canopy is fully grown ready for harvest. After harvest, between July 1st and mid-August, the average PAI of the footprint decreases in response to the 50% reduction in irrigation. Irrigation was fully stopped in mid-September, resulting in leaf rolling and a general canopy shrinkage and a decline in PAI values (Rouault et al., 2024). Between mid-August and end-September, PAI values increased as a result of multiple rain events that eased the water stress, rehydrating the canopy and allowing leaf expansion. The onset of senescence, pruning activities, and natural leaf loss during November and December resulted in a sharp decline in PAI from early October.

Figure 4b shows the difference in response for thermal and epithermal neutrons to the changes in soil moisture and vegetation development. The epithermal neutron counts exhibit a consistent and proportional response to soil moisture dynamics, with sharp dips in response to precipitation followed by a slow recovery during drydowns. In contrast, sharp dips in N_{th} are only apparent from September onwards. During three rainfall periods between April and July, thermal neutron counts do not show a clear decrease following the increase in soil moisture due to the rain. N_{th} follows the PAI more closely, increasing from dormancy through flowering and fruit set to peak canopy development. Between July and September, as the soil dries, epithermal neutron counts increase in response to decreasing soil moisture, whereas thermal neutron counts and PAI are both decreasing.

In November, thermal neutron, like epithermal neutron counts, decrease following heavy rainfall as a response to a strong increase in soil moisture. The drops in N_{th} values occur due to the increased presence of hydrogen in the recently wetted soil and intercepted water in the canopy (i.e., water droplets on leaf surfaces). While the

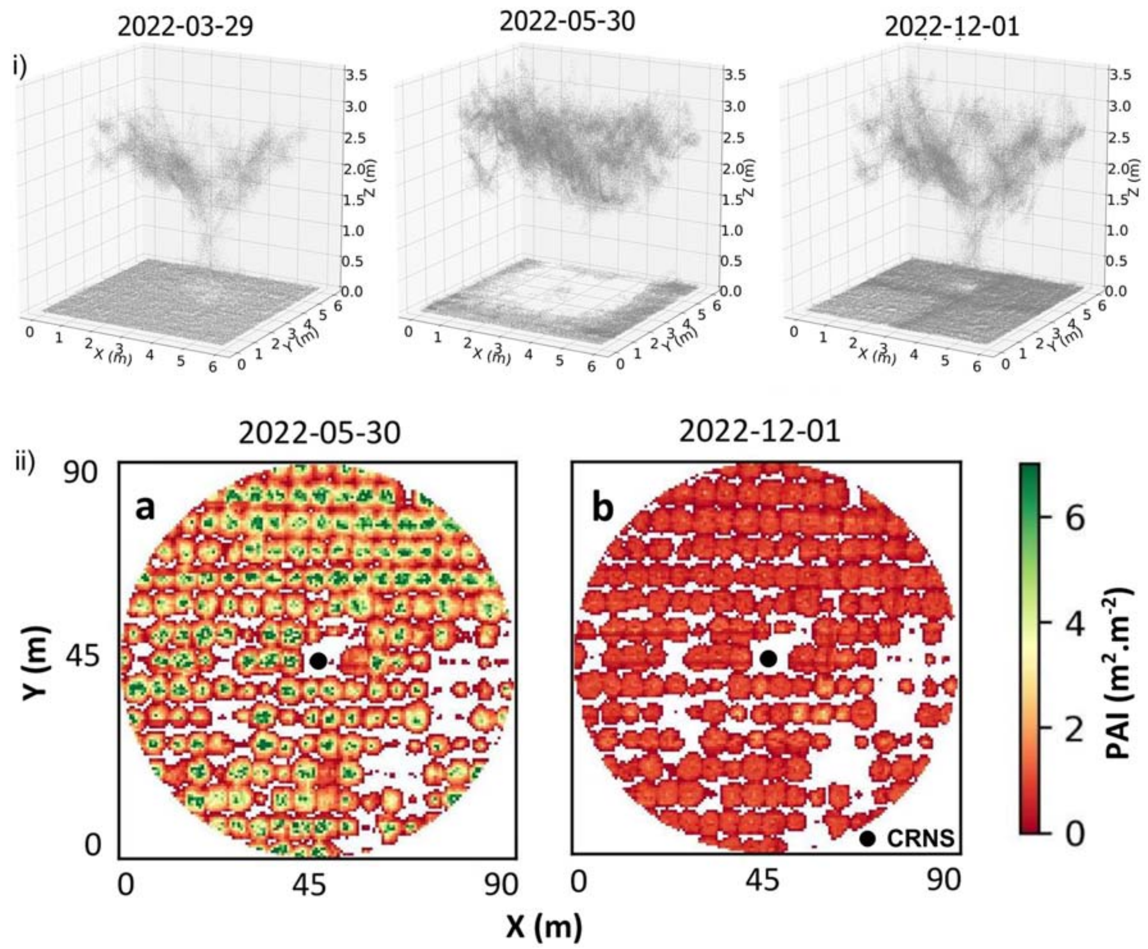

FIGURE 3
UAV LiDAR-derived PAI showing **(i)** 3D point clouds of a representative cherry tree at three phenological stages, and **(ii)** Spatial PAI distribution within the CRNS footprint (45 m radius) for **(a)** peak canopy (2022-05-30) and **(b)** leaf-off period (2022-12-01).

amount of water intercepted by vegetation is typically small (i.e., less than 2 mm) and short-lived, water puddles formed after rainfall due to soil saturation have a more significant impact by enhancing thermal neutron absorption and reducing measured count rates (Schrön et al., 2017). This leads to a temporary decorrelation between the PAI and thermal neutron measurements. After that, while epithermal neutron counts stabilize under relatively constant soil moisture conditions, thermal neutron counts continue to decrease in response to leaf falling season. Overall, during the main growing season, thermal neutron variability seems to be primarily driven by vegetation dynamics rather than soil moisture, closely following changes in PAI and visually observed indications of water stress (leaf rolling and expansion). Figure 4 shows that epithermal neutron counts respond to soil moisture changes throughout the season. Thermal neutrons only exhibit a clear response to soil moisture dynamics following significant rainfall events and during the senescence stage.

The relation of thermal and epithermal neutrons to soil moisture and vegetation are further examined in Figure 5, which presents the correlation between daily neutron counts and *in-situ* SM measurements. Figure 5a shows that N_{epi} is strongly correlated with *in situ* SM ($r = -0.95$, $R^2 = 0.91$), with data points mostly clustered along the regression line. The high R^2 value indicates that approximately 91% of the variance in N_{epi} can be explained by soil moisture alone, with limited influence of other hydrogen sources such water within the vegetation. This strong relationship explains why N_{epi} was very responsive to SM variations throughout the year, as expected from CRNS theory and existing literature.

Figure 5b shows that N_{th} has a weaker relationship with *in situ* SM ($r = -0.78$, $R^2 = 0.61$). SM clearly influences N_{th}. However, as shown in Figure 4, the response to soil moisture occurred primarily in response to very large rainfall events and during senescence. This explains why R^2 between N_{th} and SM is lower than R^2 between N_{epi} and SM.

The data points are scattered around the regression line, suggesting that other hydrogen pools are contributing to the variance. For example, in the soil moisture range (0.23–0.27 $\mathrm{m^3\ m^{-3}}$) N_{th} varies from 1,070 to 1,140 cph for similar soil moisture levels. At SM values between 0.1 and 0.2 $\mathrm{m^3\ m^{-3}}$, N_{th} varies from approximately 1,150 to 1,240 cph, a range of 90 cph. These observations suggest that variations in N_{th} during the growing season are primarily driven by something other than soil moisture fluctuations.

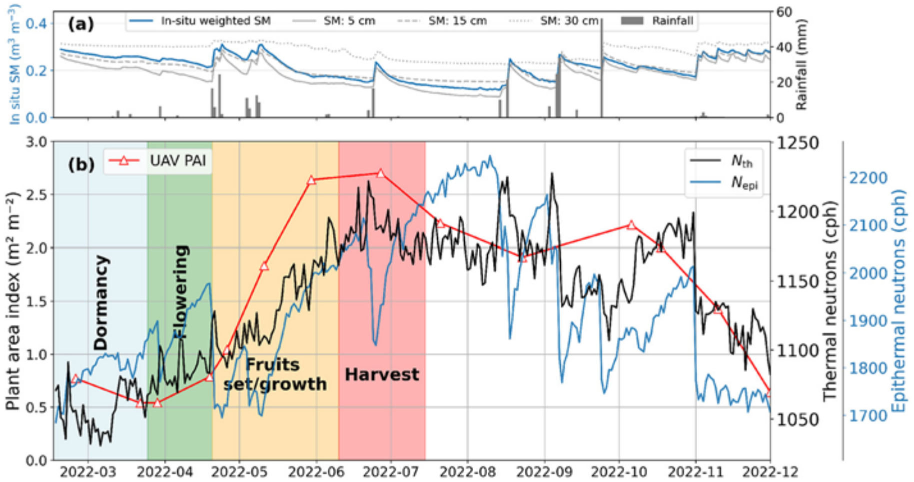

FIGURE 4
Time series showing the relationship between neutron counts, vegetation dynamics, and soil moisture. **(a)** *In-situ* soil moisture (blue line) and rainfall events (gray bars). Soil moisture (SM) at a given depth corresponds to the weighted average of the values measured in the two pits where the weights are the irrigated and non-irrigated field areas. **(b)** PAI averaged over the CRNS footprint (red line, triangles indicate measurement dates), daily N_{th} (black line), and N_{epi} (blue line). Background shading represents development phases. The figure shows the co-variation between N_{th} and PAI, while in contrast the relationship between N_{epi} and soil moisture.

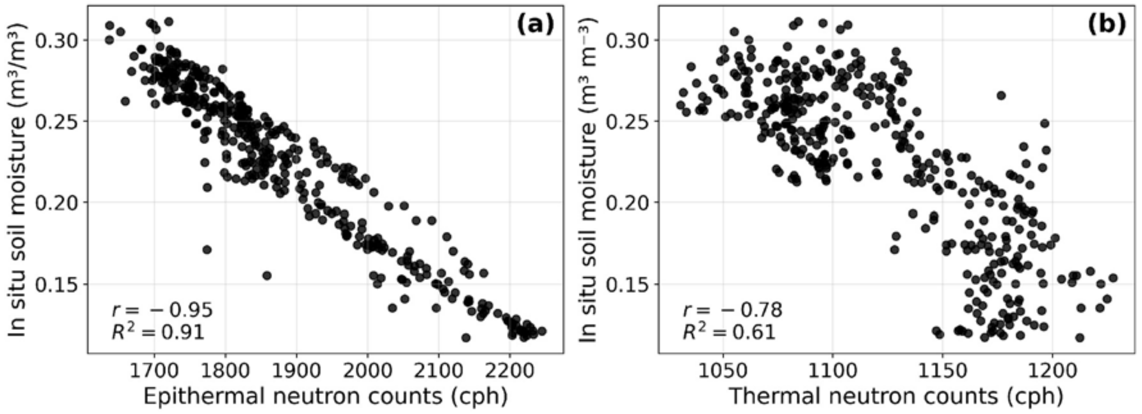

FIGURE 5
Correlation between daily neutron counts and *in-situ* soil moisture. **(a)** (N_{epi}), **(b)** (N_{th}). The stronger relationship for epithermal neutrons demonstrates minimal interference from vegetation changes.

3.3 Correlation between PAI values in the CRNS footprint and daily average neutron counts

Figure 6 shows the relationship between PAI and neutron counts, using color to indicate the time of year. Figure 6a shows that N_{th} exhibit a strong linear correlation with PAI ($R^2 = 0.86$). Increasing PAI indicates an increase in leaf and/or stem area (and volume), thereby an increase in hydrogen stored as water in the vegetation. The slope indicates that N_{th} is sensitive to this change. Figure 6b shows that the relationship between N_{epi} and PAI is weaker ($R^2 = 0.29$). This is consistent with existing literature, and the previous figure which showed that N_{epi} was primarily sensitive to soil moisture.

Note that the PAI data were resampled to 3 m resolution to match PlanetScope imagery. However, at 3 m resolution, each voxel includes both vegetation and empty ground space, which leads to a considerable number of ground returns and hence lowers the PAI estimation. Supplementary Figures S5–S7 show that the relation with thermal neutron counts remain almost unchanged regardless of resolution, and the correlation between PAI and N_{th} at 3 m voxel resolution is still high ($R^2 = 0.84$).

Following the example of Brogi et al. (2025), a LOOCV analysis was performed to test how well PAI could be predicted using thermal neutron count rates. The cross-validation yielded an R^2 of 0.73 and an RMSE of 0.4 $m^2\ m^{-2}$. This RMSE corresponds to about 14% of the observed range in PAI values (see Figure 4). The strong correlation between N_{th} and PAI suggests that N_{th} may be suitable for monitoring plant development. However, it remains important to acknowledge the potentially confounding influence of soil moisture, as reported in Figure 4.

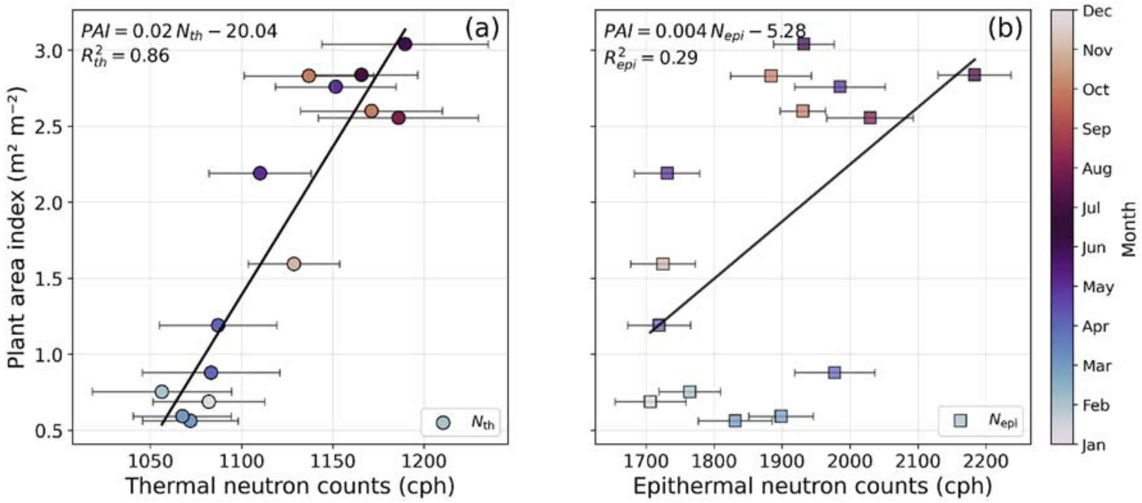

FIGURE 6
Correlation between average PAI values in the CRNS footprint and daily average neutron counts. Error bars indicate the daily standard deviation of hourly neutron count rates. **(a)** N_{th} show a strong linear relationship with PAI ($R^2 = 0.86$), with points colored by month. **(b)** N_{epi} which exhibit a weak relationship with PAI ($R^2 = 0.29$), and show that their primary sensitivity is to soil moisture rather than vegetation dynamics.

3.4 PlanetScope and Sentinel-2 vegetation indices

The vegetation index maps showed patterns consistent with the LiDAR-PAI maps, albeit at coarser resolution. As an example, Figure 7 shows NDRE maps from PlanetScope and Sentinel-2 at two distinct periods. PlanetScope-derived NDRE in Figure 7a shows a spatial distribution similar to the PAI map shown in Figure 3a with two distinct clusters of values, with lower values in the lower right quadrant. This is likely due to missing trees or recent replanting (smaller canopy size), which results in more inter-row (bare or vegetated soil) being captured by the satellite. Depending on the inter-row conditions, this surface can have lower or higher NDRE values compared to the trees. For instance, in Figure 7c, the pixels in the lower right quadrant show higher NDRE values (approximately 0.45) compared to the rest of the plot (which is around 0.3). This is likely due to the presence of grass in that quadrant, which contributes more to the vegetation indices by reflecting more in the near-infrared band compared to trees in the senescence stage (see Figure 2). Similar patterns are observed in Sentinel-2 images shown in Figures 7b, d despite their lower resolution.

3.5 Correlation between N_{th} counts and vegetation indices

Figure 8 compares the temporal variation of N_{th} and vegetation indices (NDVI, NDWI, NDRE, and LAI) averaged over the 45 m radius area of the CRNS footprint. The PlanetScope and Sentinel-2 vegetation indices capture the seasonal dynamics in the orchard, such as the stages of dormancy, growth and senescence. The dip between June and mid-August was caused by leaf rolling and stress, followed by a recovery between August and October after multiple rainfall events and a steady decline starting in October with the onset of leaf loss (Rouault et al., 2024).

For example, the NDVI shows a marked increase from 0.5 in February to 0.8 by June which reflects vegetation development during this period. This is followed by a decline to 0.63 between June and August, likely due to water stress and leaf rolling. Between August and October, the NDVI increases again, reaching values between 0.64 and 0.8, driven by rainfall and recovery. However, it decreases steadily afterward, aligning with the onset of leaf loss. PlanetScope and Sentinel-2 show globally similar trends for the various calculated vegetation indices, despite small differences in absolute values, most noticeably for LAI.

The temporal variations of the vegetation indices reveal sensitivity to environmental conditions. For example, on 26 September in Figure 8, a sudden drop in vegetation indices was observed after heavy rain in the field. Such a drop may be explained by the temporary presence of water droplets on the leaf surfaces after rainfall. When water covers the leaves, it forms a thin layer that enhances the absorption in the near-infrared band before it can be reflected, while slightly affecting the red and green bands. That reflection mechanism causes a decrease in vegetation indices based on high near-infrared and low visible reflectance (Gao et al., 2025). Differences between the indices reflect their differing sensitivity to, e.g., chlorophyll, water content, etc. Although similar dynamics are observed for the PlanetScope and Sentinel-2 images, PlanetScope provides finer spatial details and greater temporal density. As with the LiDAR-derived PAI, Figure 8 shows that N_{th} covaries with vegetation indices, with a decorrelation in the trends observed when N_{th} responds to rain events.

To allow a direct comparison, the correlation between multispectral-derived vegetation indices and N_{th} was calculated using data from the same dates when the PAI was collected, see colored points in Figure 9. Weaker correlations with N_{th}, compared to PAI, were obtained with LAI derived from Sentinel-2 ($R^2 = 0.50$) and PlanetScope ($R^2 = 0.59$), see Figure 9a. This was

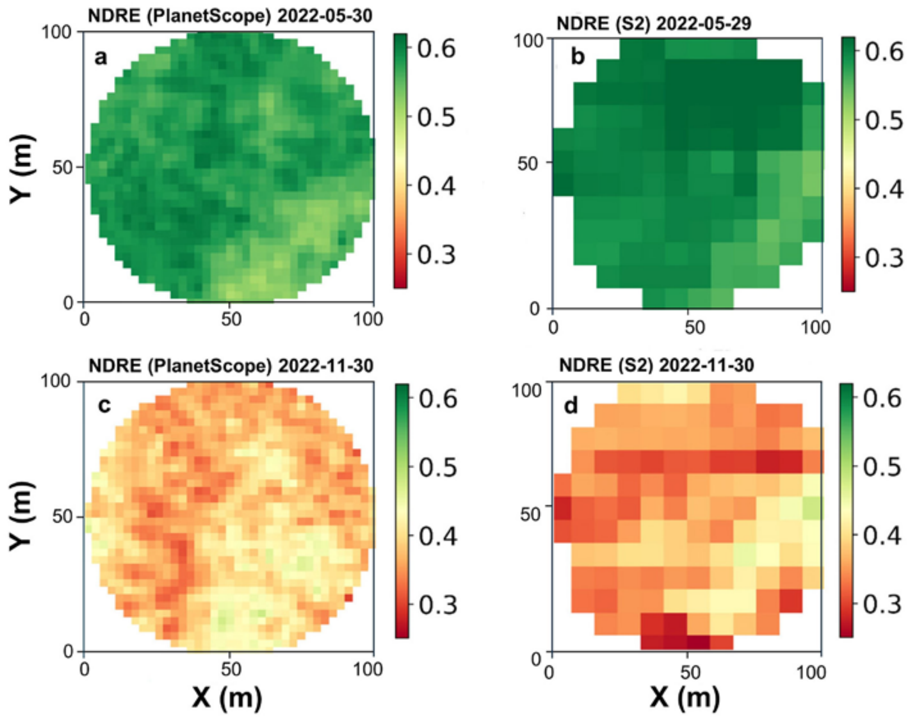

FIGURE 7
NDRE maps from PlanetScope **(a, c)** and Sentinel-2 **(b, d)** for late May (peak canopy density) and late November (leaf-off). The maps illustrate seasonal canopy changes between these periods.

expected because optical reflectance primarily captures the top surface layer of the canopy, whereas the entire canopy influences the neutron count. The correlation between N_{th} and vegetation indices is likely because the upper canopy is representative of the whole canopy. The purpose of these comparisons is to evaluate the relationship between N_{th} commonly used vegetation indices. While N_{th} has shown strong correlation with PAI in this orchard system, vegetation indices from satellite data have advantages in terms of spatial coverage and temporal frequency. Therefore, understanding how well vegetation indices correlate with N_{th} helps assess whether N_{th} could potentially complement or substitute for vegetation indices in monitoring orchard development, particularly when satellite data are limited by cloud cover or acquisition frequency. Among all of the vegetation indices examined herein, PlanetScope-derived NDRE, see Figure 9d and NDVI, Figure 9b showed the highest correlation with N_{th}, with $R^2 = 0.69$ and $R^2 = 0.61$, respectively. However, a lower correlation was observed between N_{th} and NDWI with $R^2 = 0.48$, see Figure 9c. PlanetScope-derived vegetation indices show consistently higher correlations with N_{th} compared to Sentinel-2. This is most likely due to PlanetScope's finer spatial resolution, which captures more pure pixels of vegetation compared to Sentinel-2's 10-m resolution that is more affected by mixed soil–canopy pixels.

The stronger correlation with NDRE compared to other indices is attributed to the sensitivity of the red-edge band, used in the NDRE calculation, to chlorophyll content and canopy structural characteristics. A recent study reported that the red-edge bands show the highest sensitivity (>85%) for structural leaf-parameters among multiple spectral bands (Yan et al., 2025). In contrast, Sentinel-2 LAI, NDVI, NDWI, and NDRE show similar, lower correlations with N_{th}, likely due to the uncertainties of model-based retrievals in heterogeneous orchard environments.

While the correlations presented in Figure 9 are based on dates coinciding with UAV-LiDAR acquisitions (colored points), the full temporal dataset (gray points) provides additional information about the N_{th}-vegetation index relationships. For example, the scatter in the complete dataset shows potential nonlinear, possibly saturation effects at higher vegetation index values, clearly observed in the NDVI subplot in Figure 9b where NDVI values plateau around 0.7–0.85 even as N_{th} continues to increase beyond 1,150 cph. Similar effects are observed in NDWI, as shown in Figure 9c (plateauing around 0.65–0.80), and NDRE (around 0.50–0.60). Optical indices become less sensitive to canopy changes at high biomass levels. Additionally, some of the temporal decorrelation between N_{th} and vegetation indices occurs during and immediately after rainfall events (as discussed in relation to Figure 8), which contributes to the scatter in the full dataset. The lower correlation between N_{th} and the multispectral-derived vegetation indices compared to the LiDAR-derived PAI is due to the fact that N_{th} is affected by the entire canopy while optical reflectances are mainly influenced by the top surface of the canopy.

3.6 On the confounding influence of soil moisture

Results in Figures 4, 5 indicate that while there is a high correlation between N_{th} and PAI, there is also sensitivity to soil moisture. In order to use N_{th} directly to predict PAI, a correction

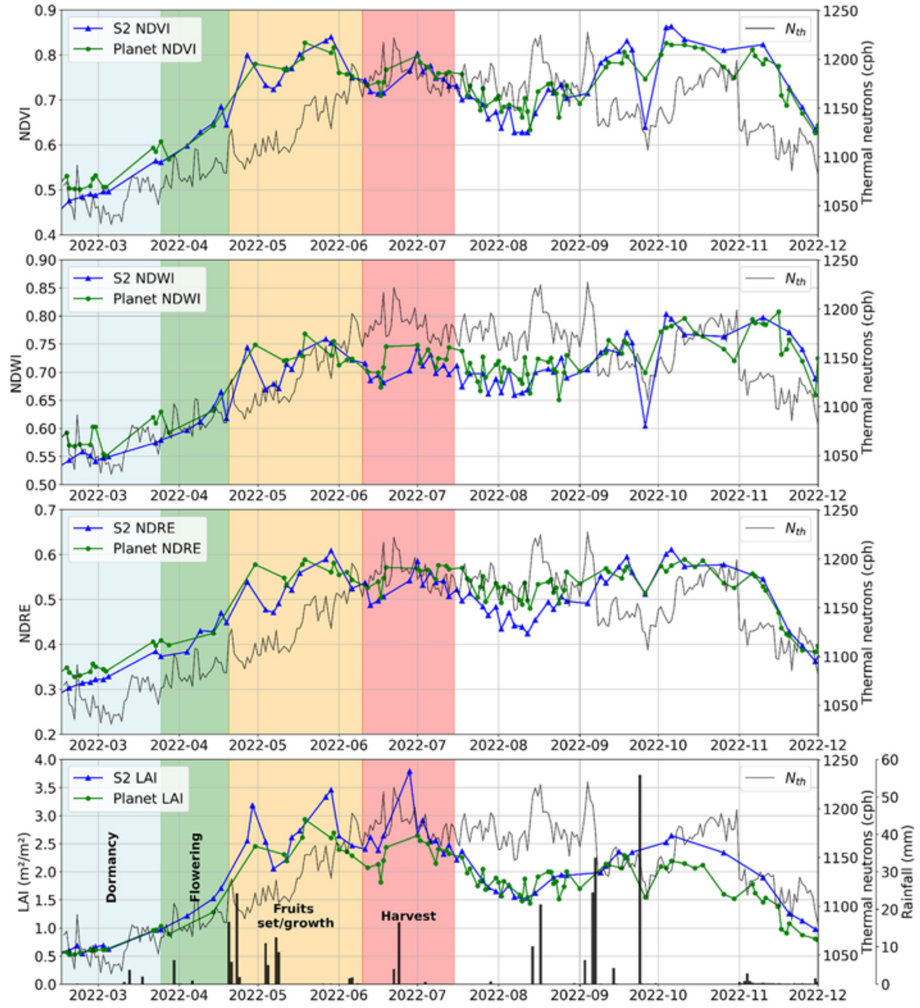

FIGURE 8
Seasonal time series of vegetation indices (NDVI, NDWI, NDRE, and LAI) from Sentinel-2 (S2) and PlanetScope satellite data for the cherry orchard in 2022, with rainfall data. The phenological stages of the cherry trees are highlighted.

would be needed to account for the effect of soil moisture on N_{th}. One solution would be to establish a correction term based on a simple fit between N_{th} and SM during a period of low PAI. Such a correction term could be applied to the time series to obtain a SM-corrected thermal signal with which to predict PAI.

Obtaining such a correction from the observations in this study is challenging due to covariance between PAI and SM (SM tends to be high when PAI is low and vice versa) and the limited SM variability during the low PAI period (See Figure 4). During this study, SM variations occurred in the period between mid-April and October, the period in which PAI and the vegetation indices are also most dynamic (Figures 4, 8). Extending the study duration provides no guarantee that soil moisture variability would be observed during a low PAI period. Therefore, relying on calibration of a simple, empirical correction term is not always practical.

Figures 5, 6 show that both N_{th} and N_{epi} depend on both SM and vegetation, which is consistent with previous studies focused on soil moisture and irrigation estimation (Jakobi et al., 2022; Brogi et al., 2023; Li et al., 2019; Baatz et al., 2015; Brogi et al., 2025; Köhli, 2026). N_{epi} is more strongly correlated with SM than with vegetation (PAI and vegetation indices in this study). Hence, N_{epi} is used for SM estimation, acknowledging that the effect of vegetation must be taken into account (Morris et al., 2024). This study showed that N_{th} is more strongly correlated with PAI and vegetation indices than with SM. Therefore, it could be useful for vegetation monitoring provided the influence of soil moisture can be taken into account.

The use of a simple, empirical correction term may be challenging due to the seasonal variation in soil moisture and its covariance with PAI. More sophisticated approaches, e.g., based on data assimilation, should be considered to exploit the complementarity of the N_{th} and N_{epi} observations.

4 Conclusion

The objective of this study was to examine the sensitivity of N_{th} to vegetation development in a commercial perennial cherry orchard. Similar to N_{epi}, N_{th} counts are influenced by both SM and PAI. While N_{epi} showed strong sensitivity to SM ($R^2 = 0.91$) and weak sensitivity to vegetation ($R^2 = 0.29$ with PAI), N_{th} showed

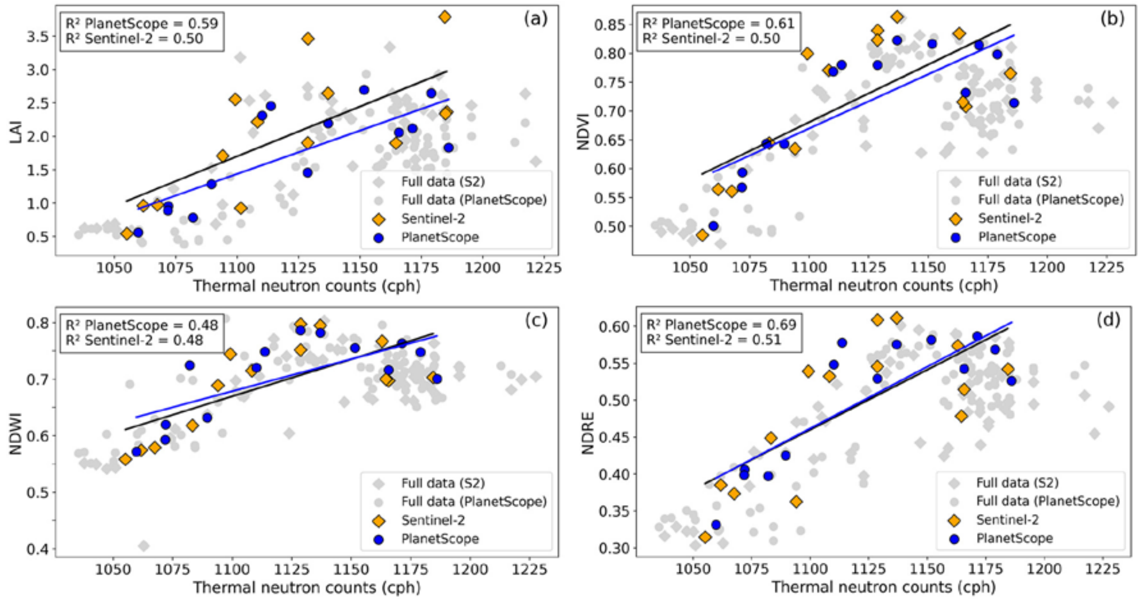

FIGURE 9
Relationships between thermal neutron counts and **(a)** LAI, **(b)** NDVI, **(c)** NDWI, and **(d)** NDRE derived from PlanetScope and Sentinel-2. Colored points indicate the selected regression dataset; gray points represent the full dataset.

a stronger correlation with vegetation descriptors than with SM. Specifically, the relationship between N_{th} and vegetation ($R^2 = 0.86$ with UAV LiDAR-derived PAI; $R^2 = 0.69$ with PlanetScope NDRE) was clearer than that between N_{th} and SM ($R^2 = 0.61$).

Results suggest that the N_{th} could be useful for vegetation monitoring. Time series of N_{th} clearly follow PAI and vegetation indices that reflect vegetation development. However, SM makes a considerable contribution to the unexplained variance and needs to be taken into account. Disentangling SM and vegetation is further complicated by covariance between SM and vegetation development. In this study, the limited variation of soil moisture during the low PAI makes it impossible to calibrate a simple "soil moisture correction" to apply to the time series. A more sophisticated approach is needed that can exploit, for example, the clear relationship between N_{epi} and SM and the complementarity of N_{th} and N_{epi}.

Exploiting the sensitivity of N_{th} to PAI, either alone or in combination with N_{epi} is potentially useful in agricultural monitoring and soil moisture estimation. In agricultural monitoring, it could enable continuous, non-invasive vegetation monitoring in orchard systems where UAV or satellite observations are limited. This capability is valuable for assessing phenological development, monitor the effect of water stress, and contributing to yield prediction and agricultural decision-making. In CRNS applications, it could be exploited in biomass corrections in soil moisture retrievals based on N_{epi}. Since many CRNS installations already record thermal neutrons alongside epithermal neutrons, this represents an opportunity to enhance the value of existing networks. Additional studies are needed to extend this analysis to other orchard types, vegetation structures, and climatic conditions, and to assess if combined use of N_{th} and N_{epi} to jointly consider soil and vegetation can further improve soil-moisture estimation in operational CRNS networks.

Data availability statement

The raw data supporting the conclusions of this article will be made available by the authors, without undue reservation.

Author contributions

SA-M: Conceptualization, Data curation, Formal analysis, Methodology, Validation, Visualization, Writing – original draft, Writing – review & editing. SS-D: Investigation, Supervision, Validation, Writing – review & editing. ME: Conceptualization, Supervision, Writing – review & editing. OV: Data curation, Software, Validation, Visualization, Writing – review & editing. OC: Data curation, Project administration, Software, Writing – review & editing. GP: Data curation, Software, Writing – review & editing. CD: Conceptualization, Investigation, Supervision, Writing – review & editing. DC: Investigation, Resources, Supervision, Writing – review & editing. MM: Funding acquisition, Investigation, Project administration, Resources, Supervision, Writing – review & editing.

Funding

The author(s) declared that financial support was received for this work and/or its publication. The research reported in this publication was funded by King Abdullah University of Science and Technology (KAUST).

Acknowledgments

The authors thank Mr. Aubery, the owner of the farm, for granting access and permission to install instruments on the site. We also thank Jorge Rodriguez Galvis and Victor Angulo Morales for their guidance in creating some of the figures used in this study.

Conflict of interest

The author(s) declared that this work was conducted in the absence of any commercial or financial relationships that could be construed as a potential conflict of interest.

The authors MM and ME declared that they were an editorial board member of Frontiers at the time of submission. This had no impact on the peer review process and the final decision.

Generative AI statement

The author(s) declared that generative AI was not used in the creation of this manuscript.

Publisher's note

Supplementary material

The Supplementary Material for this article can be found online at: https://www.frontiersin.org/articles/10.3389/frwa.2026.1749654/full#supplementary-material

References

Abubakar, M. A., Chanzy, A., Flamain, F., and Courault, D. (2023). Characterisation of grapevine canopy leaf area and inter-row management using Sentinel-2 time series. *OENO One* 57, 1–13. doi: 10.20870/oeno-one.2023.57.4.7703

Agisoft (2024). *Agisoft Metashape*. Available online at: https://www.agisoft.com (Accessed February 2, 2026).

Al-Mashharawi, S. K., Steele-Dunne, S. C., El Hajj, M. M., Schrön, M., Doussan, C., Courault, D., et al. (2025). Accounting for biomass water equivalent variations in soil moisture retrievals from cosmic ray neutron sensor. *Agric. Water Manag.* 313:109493. doi: 10.1016/j.agwat.2025.109493

Almeida, D. R. A. D., Stark, S. C., Silva, C. A., Hamamura, C., and Valbuena, R. (2021). *leafR: Calculates the Leaf Area Index (LAD) and Other Related Functions. R Package Version 0.3.5*. Available online at: https://github.com/draalmeida/leafr (Accessed February 2, 2026).

Andreasen, M., Jensen, K. H., Bogena, H., Desilets, D., Zreda, M., Looms, M. C., et al. (2020). Cosmic ray neutron soil moisture estimation using physically based site-specific conversion functions. *Water Resour. Res.* 56:e2019WR026588. doi: 10.1029/2019WR026588

Andreasen, M., Jensen, K. H., Desilets, D., Zreda, M., Bogena, H. R., Looms, M. C., et al. (2017). Cosmic-ray neutron transport at a forest field site: the sensitivity to various environmental conditions with focus on biomass and canopy interception. *Hydrol. Earth Syst. Sci.* 21, 1875–1894. doi: 10.5194/hess-21-1875-2017

Andreasen, M., Jensen, K. H., Zreda, M., Desilets, D., Bogena, H., Looms, M. C., et al. (2016). Modeling cosmic ray neutron field measurements. *Water Resour. Res.* 52, 6451–6471. doi: 10.1002/2015WR018236

Baatz, R., Bogena, H. R., Hendricks Franssen, H.-J., Huisman, J. A., Montzka, C., Vereecken, H., et al. (2015). An empirical vegetation correction for soil water content quantification using cosmic ray probes. *Water Resour. Res.* 51, 2030–2046. doi: 10.1002/2014WR016443

Baldin, C. M., and Casella, V. M. (2024). Vegetative index intercalibration between PlanetScope and Sentinel-2 through a SkySat classification in the context of "Riserva San Massimo" rice farm in Northern Italy. *Remote Sens.* 16:3921. doi: 10.3390/rs16213921

Baroni, G., and Oswald, S. (2015). A scaling approach for the assessment of biomass changes and rainfall interception using cosmic-ray neutron sensing. *J. Hydrol.* 525, 264–276. doi: 10.1016/j.jhydrol.2015.03.053

Bogena, H. R., Huisman, J. A., Baatz, R., Hendricks Franssen, H.-J., and Vereecken, H. (2013). Accuracy of the cosmic-ray soil water content probe in humid forest ecosystems: the worst case scenario. *Water Resour. Res.* 49, 5778–5791. doi: 10.1002/wrcr.20463

Bogena, H. R., Schrön, M., Jakobi, J., Ney, P., Zacharias, S., Andreasen, M., et al. (2022). COSMOS-Europe: a European network of cosmic-ray neutron soil moisture sensors. *Earth Syst. Sci. Data* 14, 1125–1151. doi: 10.5194/essd-14-1125-2022

Bouvier, M., Durrieu, S., Fournier, R. A., and Renaud, J.-P. (2015). Generalizing predictive models of forest inventory attributes using an area-based approach with airborne LiDAR data. *Remote Sens. Environ.* 156, 322–334. doi: 10.1016/j.rse.2014.10.004

Brogi, C., Jakobi, J., Huisman, J., Schmidt, M., Montzka, C., Bates, J., et al. (2025). Cosmic-ray neutron sensors provide scale-appropriate soil water content and vegetation observations for eddy covariance stations in agricultural ecosystems. *Agric. For. Meteorol.* 373:110731. doi: 10.1016/j.agrformet.2025.110731

Brogi, C., Pisinaras, V., Köhli, M., Dombrowski, O., Hendricks Franssen, H.-J., Babakos, K., et al. (2023). Monitoring irrigation in small orchards with cosmic-ray neutron sensors. *Sensors* 23:2378. doi: 10.3390/s23052378

Contreras, F., Cayuela, M. L., Sánchez-Monedero, M. A., and Pérez-Cutillas, P. (2025). Multi-source remote sensing for large-scale biomass estimation in mediterranean olive orchards using GEDI LiDAR and Machine Learning. *EGUsphere* 2025, 1–27. doi: 10.5194/bg-22-7625-2025

Cooper, H. M., Bennett, E., Blake, J., Blyth, E., Boorman, D., Cooper, E., et al. (2021). COSMOS-UK: national soil moisture and hydrometeorology data for environmental science research. *Earth Syst. Sci. Data* 13, 1737–1757. doi: 10.5194/essd-13-1737-2021

Courault, D., Hossard, L., Demarez, V., Dechatre, H., Irfan, K., Baghdadi, N., et al. (2021). STICS crop model and Sentinel-2 images for monitoring rice growth and yield in the Camargue region. *Agron. Sustain. Dev.* 41:17. doi: 10.1007/s13593-021-00697-w

CSIRO (2010). *COSMOS-OZ: Australia's Cosmic-Ray Soil Moisture Monitoring Network*. Available online at: https://cosmoz.csiro.au/ (Accessed October 15, 2025).

DJI Technology Co., Ltd. (2019). *DJI Zenmuse P1 RGB Camera*. Shenzhen: DJI Technology Co., Ltd. Available online at: https://www.dji.com/zenmuse-p1 (Accessed February 2, 2026).

DJI Technology Co., Ltd. (2020). *DJI Matrice 300 RTK Quadcopter*. Shenzhen: DJI Technology Co., Ltd. Available online at: https://www.dji.com/de/support/product/matrice-300 (Accessed February 2, 2026).

DJI Technology Co., Ltd. (2021). *DJI L1 LiDAR Sensor*. Shenzhen: DJI Technology Co., Ltd. Available online at: https://www.dji.com/de/support/product/zenmuse-l1 (Accessed February 2, 2026).

Dorigo, W. A., Gruber, A., de Jeu, R. A. M., Wagner, W., Stacke, T., Loew, C., et al. (2021). The International Soil Moisture Network: serving Earth system science for over a decade. *Hydrol. Earth Syst. Sci.* 25, 5749–5804. doi: 10.5194/hess-25-5749-2021

European Space Agency (2020). *Sentinel-2 User Handbook*. Available online at: https://sentinel.esa.int/documents/247904/685211/Sentinel-2_User_Handbook (Accessed December 19, 2024).

Farhan, S. M., Yin, J., Chen, Z., and Memon, M. S. (2024). A comprehensive review of LiDAR applications in crop management for precision agriculture. *Sensors* 24:5409. doi: 10.3390/s24165409

Franz, T. E., Wahbi, A., and Avery, W. (2018). "Chapter 4: Estimation of biomass water equivalent via the cosmic ray neutron sensor," in *Cosmic Ray Neutron Sensing: Estimation of Agricultural Crop Biomass Water Equivalent*, eds. A. Wahbi, L. Heng, and G. Dercon (Springer International Publishing), 25–32. doi: 10.1007/978-3-319-69539-6_4

Gao, S., Yan, K., Yan, G., Rautiainen, M., Knyazikhin, Y., Myneni, R. B., et al. (2025). Rainfall-caused water film on canopy surface biases remotely-sensed vegetation greenness. *Remote Sens. Environ.* 324:114747. doi: 10.1016/j.rse.2025.114747

Grau, E., Durrieu, S., Fournier, R., Gastellu-Etchegorry, J.-P., and Yin, T. (2017). Estimation of 3D vegetation density with terrestrial laser scanning data using voxels. A sensitivity analysis of influencing parameters. *Remote Sens. Environ.* 191, 373–388. doi: 10.1016/j.rse.2017.01.032

Hagolle, O., Dedieu, G., Mougenot, B., Debaecker, V., Duchemin, B., Meygret, A., et al. (2008). Correction of aerosol effects on multitemporal images acquired with constant viewing angles: application to Formosat-2 images. *Remote Sens. Environ.* 112, 1689–1701. doi: 10.1016/j.rse.2007.08.016

Houborg, R., and McCabe, M. F. (2016). Adapting a regularized canopy reflectance model (REGFLEC) for the retrieval challenges of dryland agricultural systems. *Remote Sens. Environ.* 186, 105–120. doi: 10.1016/j.rse.2016.08.017

Houborg, R., and McCabe, M. F. (2018). A cubesat enabled spatio-temporal enhancement method (CESTEM) utilizing Planet, Landsat and MODIS data. *Remote Sens. Environ.* 209, 211–226. doi: 10.1016/j.rse.2018.02.067

Hydroinnova LLC (2024). *CRS1000: Cosmic Ray Soil Moisture Probe Manual, Version 3*. Available online at: https://hydroinnova.com/_downloads/CRS1000_v3.pdf (Accessed November 4, 2024).

International Soil Moisture Network (2025). *COSMOS Network*. Available online at: https://ismn.earth/en/networks/?id=COSMOS (Accessed February 2, 2026).

Jakobi, J., Huisman, J. A., Fuchs, H., Vereecken, H., and Bogena, H. R. (2022). Potential of thermal neutrons to correct cosmic-ray neutron soil moisture content measurements for dynamic biomass effects. *Water Resour. Res.* 58:e2022WR031972. doi: 10.1029/2022WR031972

Jakobi, J., Huisman, J. A., Köhli, M., Rasche, D., Vereecken, H., Bogena, H. R., et al. (2021). The footprint characteristics of cosmic ray thermal neutrons. *Geophys. Res. Lett.* 48:e2021GL094281. doi: 10.1029/2021GL094281

Jakobi, J., Huisman, J. A., Vereecken, H., Diekkrüger, B., and Bogena, H. R. (2018). Cosmic ray neutron sensing for simultaneous soil water content and biomass quantification in drought conditions. *Water Resour. Res.* 54, 7383–7402. doi: 10.1029/2018WR022692

Jonckheere, I., Fleck, S., Nackaerts, K., Muys, B., Coppin, P., Weiss, M., et al. (2004). Review of methods for *in situ* leaf area index determination: part I. Theories, sensors and hemispherical photography. *Agric. For. Meteorol.* 121, 19–35. doi: 10.1016/j.agrformet.2003.08.027

Kington, J., and Collison, A. (2022). *PlanetScope Scene Level Normalization of Planet Dove Imagery*. Technical Report, Planet Labs Inc., San Francisco, CA, United States.

Köhli, M. (2026). Soil moisture measurements by cosmic-ray neutron sensing: a critical review. *Geoderma* 465:117626. doi: 10.1016/j.geoderma.2025.117626

Li, D., Schrön, M., Köhli, M., Bogena, H., Weimar, J., Jiménez Bello, M. A., et al. (2019). Can drip irrigation be scheduled with cosmic-ray neutron sensing? *Vadose Zone J.* 18:190053. doi: 10.2136/vzj2019.05.0053

McJannet, D. L., and Desilets, D. (2023). Incoming neutron flux corrections for cosmic-ray soil and snow sensors using the global neutron monitor network. *Water Resour. Res.* 59:e2022WR033889. doi: 10.1029/2022WR033889

Morris, T. C., Franz, T. E., Becker, S. M., and Suyker, A. E. (2024). Effect of biomass water dynamics in cosmic-ray neutron sensor observations: a long-term analysis of maize–soybean rotation in Nebraska. *Sensors* 24:4094. doi: 10.3390/s24134094

Mukhtar, A., Andre, C., Guillaume, P., Fabrice, F., and Dominique, C. (2022). Detection of irrigated permanent grasslands with sentinel-2 based on temporal patterns of the leaf area index (LAI). *Remote Sens.* 14:3056. doi: 10.3390/rs14133056

Panumonwatee, G., Choosumrong, S., Pampasit, S., Premprasit, R., Nemoto, T., and Raghavan, V. (2025). Machine learning technique for carbon sequestration estimation of mango orchards area using Sentinel-2 Data. *Carbon Res.* 4:33. doi: 10.1007/s44246-025-00201-z

Planet Labs Inc. (2023). *PlanetScope Scene Product Specification*. Available online at: https://assets.planet.com/docs/Planet_PSScene_Imagery_Product_Spec_letter_screen.pdf (Accessed February 2, 2026).

Rasche, D., Weimar, J., Schrön, M., Köhli, M., Morgner, M., Güntner, A., et al. (2023). A change in perspective: downhole cosmic-ray neutron sensing for the estimation of soil moisture. *Hydrol. Earth Syst. Sci.* 27, 3059–3082. doi: 10.5194/hess-27-3059-2023

Rosolem, R., Shuttleworth, W. J., Zreda, M., Franz, T. E., Zeng, X., Kurc, S. A., et al. (2013). The effect of atmospheric water vapor on neutron count in the cosmic-ray soil moisture observing system. *J. Hydrometeorol.* 14, 1659–1671. doi: 10.1175/JHM-D-12-0120.1

Rouault, P., Courault, D., Pouget, G., Flamain, F., Diop, P.-K., Desfonds, V., et al. (2024). Phenological and biophysical mediterranean orchard assessment using ground-based methods and sentinel 2 data. *Remote Sens.* 16:3393. doi: 10.3390/rs16183393

Schrön, M., Köhli, M., Scheiffele, L., Iwema, J., Bogena, H. R., Lv, L., et al. (2017). Improving calibration and validation of cosmic-ray neutron sensors in the light of spatial sensitivity. *Hydrol. Earth Syst. Sci.* 21, 5009–5030. doi: 10.5194/hess-21-5009-2017

Schrön, M., Rasche, D., Weimar, J., Köhli, M., Herbst, K., Boehrer, B., et al. (2024). Buoy-based detection of low-energy cosmic-ray neutrons to monitor the influence of atmospheric, geomagnetic, and heliospheric effects. *Earth Space Sci.* 11:e2023EA003483. doi: 10.1029/2023EA003483

Tian, L., Wu, X., Tao, Y., Li, M., Qian, C., Liao, L., et al. (2023). Review of remote sensing-based methods for forest aboveground biomass estimation: progress, challenges, and prospects. *Forests* 14:1086. doi: 10.3390/f14061086

Tian, Z., Li, Z., Liu, G., Li, B., and Ren, T. (2016). Soil water content determination with cosmic-ray neutron sensor: correcting aboveground hydrogen effects with thermal/fast neutron ratio. *J. Hydrol.* 540, 923–933. doi: 10.1016/j.jhydrol.2016.07.004

Upadhyaya, D. B., Evans, J., Muddu, S., Tomer, S. K., Al Bitar, A., Yeggina, S., et al. (2021). The Indian COSMOS Network (ICON): validating L-band remote sensing and modelled soil moisture data products. *Remote Sens.* 13:537. doi: 10.3390/rs13030537

Vather, T., Everson, C. S., and Franz, T. E. (2020). The applicability of the cosmic ray neutron sensor to simultaneously monitor soil water content and biomass in an *Acacia mearnsii* forest. *Hydrology* 7:48. doi: 10.3390/hydrology7030048

Wang, Q., Shi, L., Zhao, X., and Fan, J. (2023). Effects of biomass and soil water content distribution on cosmic ray neutron probe measurement. *Water* 15:2766. doi: 10.3390/w15152766

Weiss, M., Baret, F., Leroy, M., Hautecœur, O., Bacour, C., Prévot, L., et al. (2002). Validation of neural net techniques to estimate canopy biophysical variables from remote sensing data. *Agronomie* 22, 547–553. doi: 10.1051/agro:2002036

Yan, K., Gao, S., Yan, G., Ma, X., Chen, X., Zhu, P., et al. (2025). A global systematic review of the remote sensing vegetation indices. *Int. J. Appl. Earth Obs. Geoinf.* 139:104560. doi: 10.1016/j.jag.2025.104560

Zreda, M., Shuttleworth, W. J., Zeng, X., Zweck, C., Desilets, D., Franz, T., et al. (2012). COSMOS: the COsmic-ray soil moisture observing system. *Hydrol. Earth Syst. Sci.* 16, 4079–4099. doi: 10.5194/hess-16-4079-2012